ARTICLE   OPEN

Check for updates

Monolithically printed all-organic flexible photosensor active matrix

Luis Arturo Ruiz-Preciado[1,2,6], Sanghoon Baek (ID)[1,2,3,6], Noah Strobel[1,2], Kai Xia (ID)[1,2], Mervin Seiberlich (ID)[1,2], Sung-min Park (ID)[3], Uli Lemmer[1,2,4], Sungjune Jung (ID)[3,5✉] and Gerardo Hernandez-Sosa (ID)[1,2,4✉]

Upcoming technologies in the fields of flexible electronics require the cost-efficient fabrication of complex circuitry in a streamlined process. Digital printing techniques such as inkjet printing can enable such applications thanks to their inherent freedom of design permitting the mask-free deposition of multilayer optoelectronic devices without the need for subtracting techniques. Here we present an active matrix sensor array comprised of 100 inkjet-printed organic thin film transistors (OTFTs) and organic photodiodes (OPDs) monolithically integrated onto the same ultrathin substrate. Both the OTFTs and OPDs exhibited high-fabrication yield and state-of-the-art performance after the integration process. By scaling of the OPDs, we achieved integrated pixels with power consumptions down to 50 nW at one of the highest sensitivities reported to date for an all-organic integrated sensor. Finally, we demonstrated the application potential of the active matrix by static and dynamic spatial sensing of optical signals.

INTRODUCTION

Light detection is essential in present-day automotive, security, communications, healthcare, and consumer electronics technologies[1,2]. Furthermore, the growing trend of scientific advances towards key technological areas such as the internet of things and personalized healthcare is currently demanding integrative solutions based on multi-device sensing systems. Of particular interest are design concepts that cannot be accomplished with conventional silicon electronics, such as flexible, stretchable, low weight, or semi-transparent devices that can adapt to dynamic surfaces[3–5]. Such systems will play a crucial role in next-generation applications for medical and industrial monitoring or biometric identification, to augmented and virtual reality[6–13].

Organic materials offer complementary properties to silicon-based technologies thanks to the possibility of tailoring, optoelectronic, mechanical, and processing properties through chemical design[14–17]. Furthermore, their solution-processability have opened opportunities for the fabrication of (opto) electronic thin-film devices via cost-efficient printing technologies. In particular, printed optical detectors such as organic photodiodes (OPDs) and organic thin film transistors (OTFTs) have shown tremendous progress in recent years yielding performance comparable to inorganic counterparts[18,19].

Optical systems for multichannel detection are typically composed of an array of devices in which a photodiode is followed by at least one transistor which acts as a switch to activate or read the device. This so-called active-matrix configuration, facilitates control over individual pixels and therefore allows for high-device integration with minimized crosstalk[16,20]. Thus being superior in performance to passive arrays where a subsequent reading of diode-only rows and columns limits detection speed and increases the risk of electrical and optical crosstalk[21]. Recent reports on the active-matrix integration of organic-based light sensors have yielded proof of concept applications as well as first commercial examples in the fields of sensing, security, and communication[10,22–37]. However, most of these examples have employed a variety of vacuum and non-easily scalable techniques, such as thermal evaporation, spin-coating, photolithography, or the integration of organic devices with Si-backplane[23,33,34]. Whereas previous works do recognize the advantages of solution-processed devices, they have mostly been limited to the use of deposition non-patterned coating techniques[25,36,37]. The fabrication of all-organic multi-device systems employing up-scalable industrially relevant techniques for the integration of OPDs and OTFTs has only been explored in a few works[24,27]. To date the challenges to fabricate fully printed systems require to establish a robust process that ensures process compatibility of the respective OTFT and OPD material sets while yielding reliable and uniform performance over a large number of devices.

Digital printing techniques such as inkjet printing could help addressing these shortcomings while also enabling the mask-free deposition of multilayer optoelectronic devices[3,18,38–40]. In contrast to coating techniques, its drop-on-demand nature allows for patterning with the μm-scale resolution, cost-efficient of production, and low-waste generation[41]. Multi-device systems such as photosensor active-matrix arrays would benefit from its inherent freedom of design and fast prototyping capabilities by minimizing iterative steps of a complex fabrication process involving multiple fabrication tools. Furthermore, inkjet printing would offer the required physical detachment between adjacent pixels, yielding lower crosstalk paths over large areas without the need for subtractive techniques[18].

In this work, we present the monolithic integration of OPDs and OTFTs by inkjet printing onto an ultrathin mechanically flexible substrate. The active-matrix array is comprised of 10×10 OTFT/ OPD optical sensors exhibiting a uniform state-of-the-art

[1]Light Technology Institute, Karlsruhe Institute of Technology, Engesserstr. 13, 76131 Karlsruhe, Germany. [2]InnovationLab, Speyererstr. 4, 69115 Heidelberg, Germany. [3]Department of Convergence IT Engineering, Pohang University of Science and Technology, 77 Cheongam-Ro, Pohang 37673, Republic of Korea. [4]Institute of Microstructure Technology, Karlsruhe Institute of Technology, Hermann-von-Helmholtz-Platz 1, 76344 Eggenstein-Leopoldshafen, Germany. [5]Department of Materials Science and Engineering, Pohang University of Science and Technology, 77 Cheongam-Ro, Pohang 37673, Republic of Korea. [6]These authors contributed equally: Luis Arturo Ruiz-Preciado, Sanghoon Baek. ✉email: sjjung@postech.ac.kr; gerardo.sosa@kit.edu

performance. Facilitated by the design flexibility of digital printing, the scaling of the geometrical footprint of the devices yielded pixels with power consumptions down to 50 nW at one of the highest sensitivities reported to date for all-organic integrated sensors. Finally, we demonstrated the application potential of the active matrix by static and dynamic spatial sensing. Compared to previously reported work we have developed an inkjet printing-based process to stack up to ten functional layers, while retaining state-of-the-art device functionality. The OPDs show spectral responsivities (SR) >356 mA W^{-1} and the OTFTs exhibit field-effect mobilities (μ) over 0.09 ± 0.01 cm^2 V^{-1} s^{-1} after integration. The presented work sets a basis for the streamlined integration of printed multi-device systems whose digital nature enables freedom of design and reduces processing complexity. The achieved high-device performance and the industrial relevance of the developed fabrication process will certainly contribute to enable future applications in optoelectronic technologies where freedom of design, low cost, performance, low weight, and flexibility are crucial.

RESULTS AND DISCUSSION
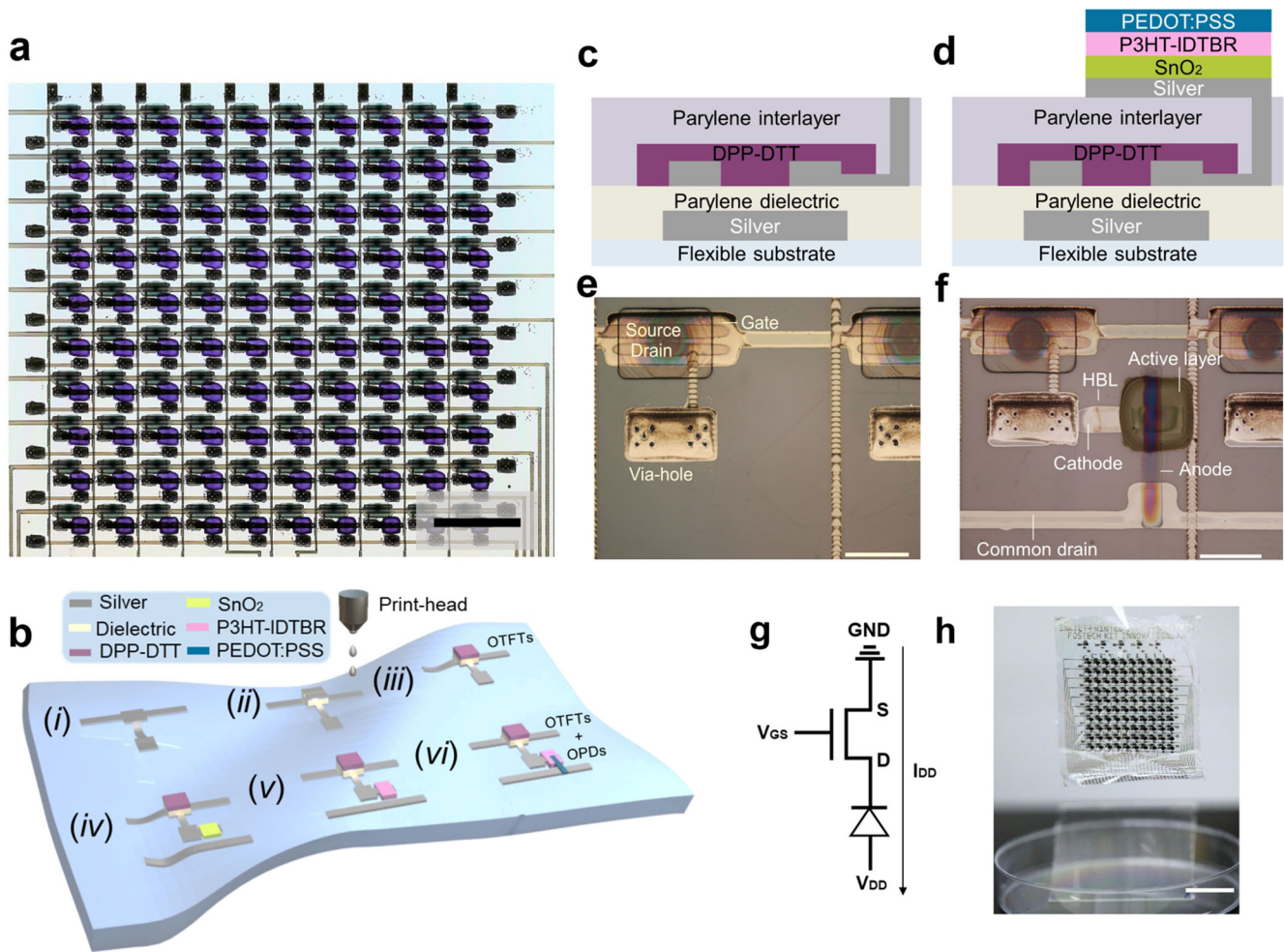### Integration, design, and fabrication
Figure 1a shows a photograph of the fabricated active-matrix sensor array comprised of 10 × 10 OPD/OTFTs pairs. In the presented layout, the anodes of all OPDs in one row are connected to a bit line, while their cathodes are connected to the corresponding transistor. The transistors are also divided into rows with their gates connecting to word lines. In this manner, the photocurrent response from the OPDs of all different pixels can be selectively retrieved using the switching behavior of the transistors. The full matrix can be read by applying a voltage that switches the transistors on and off, addressing one row at a time. Figure 1b illustrates the fabrication process of the sensor matrix where both, the OPDs and the OTFTs, were monolithically deposited on a single ultrathin parylene substrate. (i) First, the Ag gates of the OTFTs were inkjet-printed on the parylene substrate which had been previously coated on a carrier glass slide. (ii) Secondly, the Ag-based S/D electrodes were deposited on a second parylene dielectric layer covering the gate. (iii) Subsequently, the OTFT devices were completed by the deposition of poly(N-alkyl diketopyrrolopyrrole dithienylthieno-[3,2-b] thiophene) (DPP-DTT) as a semiconductor and the deposition of a parylene interlayer which served as a base for the fabrication of the OPDs. (iv) The OPDs were fabricated by inkjet printing utilizing Ag as an electrode with SnO$_2$ as hole-blocking layer, and (v) a bulk heterojunction active layer composed of poly(3-hexylthiophene) (P3HT) as a donor and the small-molecule 5,5′-[[4,4,9,9-Tetraoctyl-4,9-dihydro-s-indaceno[1,2-b:5,6-b′]dithiophene-2,7-diyl]bis(2,1,3-benzothiadiazole-7,4-diylmethylidyne)]bis[3-ethyl-2-thioxo-4-thia-zolidinone] (IDTBR) as the acceptor material. (vi) To complete the device, we inkjet-printed poly(3,4-ethylenedioxythiophene) poly-styrene sulfonate (PEDOT:PSS) as top transparent electrode. The energy level diagram of all the OPD layers is shown in Supplementary Fig. 1. Figure 1c–f show the schematic representations of the integrated device architecture and microscope images of an exemplary pixel before and after the deposition of the OPD. The images show high-quality printed layers even after the monolithic deposition of ten different layers as well as no visible degradation of the OTFT structure after the OPD is integrated. As can be seen, the devices are connected in series through a laser-drilled via-hole that connected the drain of the OTFT to the cathode of the OPD. The active area of the OPDs is defined by the overlap of the bottom silver contact with the top PEDOT:PSS contact. As schematically seen in Fig. 1g, the integrated devices can be operated by applying a driving voltage V$_{DD}$ and a gate voltage V$_{GS}$. Figure 1h illustrates the mechanical properties of the

sensor matrix. Due to having a total thickness of <5 µm, the ultra-flexible matrix could potentially allow for a broad range of flexible and wearable applications. Furthermore, the developed digital inkjet-printing deposition process could provide a large flexibility for the design of complex circuitry.

Characteristics of individual OTFTs and OPDs
As a first step, we characterized the impact of the OTFT-OPD pixel integration process on the performance of the individual devices. Figure 2 shows the figures of merit of already integrated OTFTs and OPDs measured as discrete components. Figure 2a, b show, respectively, the transfer and output characteristics of a typical OTFT after the deposition of the OPD. The voltages V$_{GS}$ and V$_{DS}$ were used to address the transistors individually (see Fig. 1g). The OTFT with width-to-length ratio W/L = 25 showed an on-current (I$_{ON}$) of ~1 µA and an off-current (I$_{OFF}$) of ~7 pA. The absence of hysteresis indicates a stable device with low charge trapping. Supplementary Fig. 2 shows the transfer characteristics in the saturation regime (V$_{DS} = -10$ V) before and after the integration showing no substantial degradation in electrical performance after printing the OPD. The frequency response of the printed OTFTs was evaluated by measuring the gate capacitance of the OTFTs while applying sinusoidal gate pulses with different frequencies. The cut-off frequency of the OTFTs was estimated to be ~200 kHz (Supplementary Fig. 3). Averaged over ten randomly selected devices, the OTFTs exhibited a threshold voltage (V$_{TH}$) of -1.2 ± 0.13 V and a μ of 0.09 ± 0.01 cm^2 V^{-1} s^{-1}. These character-istics illustrate the reliable operation of the OTFTs after under-going the integration process. Furthermore, the devices present comparable performance to previous literature reports by ours and other research groups utilizing DPP-DTT as a semiconductor[9,42].

Figure 2c shows the J-V characteristics of a photodiode with an active area of 0.11 mm^2 after being integrated onto the OTFT. The voltage V$_{diode}$, i.e., between anode and cathode, was used to address the photodiodes separately. The device was measured in the dark and under monochromatic illumination ($\lambda = 520$ nm) at light intensities up to 15 mW cm^{-2}. Measurements over ten devices showed an average dark current of 1.3 ± 0.12 µA cm^{-2} at the maximum measured V$_{diode}$ of -3 V. These values demonstrate the good quality of the printed layers, showing suppression of shunts and a good charge-blocking behavior. Figure 2d shows that the current of the OPDs increases linearly with light intensity exhibiting a linear dynamic range (LDR) of 89 dB when biased at -2 V. Figure 2e shows the SR obtained at a V$_{diode} = 0$ and -2 V for a representative OPD integrated onto one of the OTFTs. The SR shows the typical spectral bands of both materials forming the active layer (i.e., P3HT:IDTBR) extending from the visible to the near-infrared (NIR) range. When increasing V$_{diode}$ from 0 to -2 V, we observed an increment in the peak SR ($\lambda = 760$ nm) from 312 to 356 mA W^{-1}. These SR values are in accordance with that of state-of-the-art printed devices utilizing the same material system[43,44]. The 3$_{dB}$-bandwidth (i.e., detection speed) of the OPD is presented in Fig. 2f. The dynamic characteristics show a 3$_{dB}$ cut-off frequency >1 MHz at -2 V. The high 3$_{dB}$-bandwithdt suggests a favorable interplay between the RC-constant and transit time of the device stemming from a relatively small active area (0.11 mm^2) and an optimized active layer thickness (~250 nm)[43]. The specific detectivity (D*) of the device was calculated from frequency-dependent noise measurements. As shown in Supplementary Fig. 4 the device exhibits a D* of up to 3.9×10^{10} Jones at -2 V. Overall, the obtained high performance of the integrated OPDs is comparable to that of other advanced organic photodetectors devices reported in literature[13,14,44–51].

Fig. 1 Integration, design, and fabrication. a Layout of the 10×10 active-matrix array (scale bar = 5 mm). **b** Schematic of the fabrication process for the monolithic integration of inkjet-printed OTFTs and inkjet-printed OPDs on a single and flexible substrate. **c** Schematic diagram of a material stack of the OTFTs. **d** Schematic diagram of a material stack of the OTFTs plus OPDs. The connection between both devices is achieved through a via-hole. **e** Microscope images of the inkjet-printed devices for OTFT alone (scale bar = 1000 µm). **f** Microscope images of the inkjet-printed devices for OTFT plus OPD (scale bar = 1000 µm). **g** Schematic of the electric circuit. The OTFT and OPD devices are connected in series. **h** Photograph of final active-matrix sample on ultrathin (<5 µm) flexible substrate (scale bar = 20 mm).

Investigation of size and the operational voltage

The state-of-the-art performance of both the OTFTs and OPDs demonstrates the successful establishment of a robust printing integration process. Therefore, we focused on controlling the performance of the integrated system via the optimization of OPD geometry and adjustment of operational voltages while keeping the OTFT design constant. The variation in OPD active area is aimed to gain control over the photoconductance range of the pixel. By regulating V_{DD} we can then maximize the photoresponse (I_{DD}) and optimize the power consumption of the pixel. Figure 3 shows the transfer characteristics in the saturation ($V_{DD} = -10$ V) and linear ($V_{DD} = -1$ V) regime of the integrated devices utilizing OPDs active areas between 0.04 and 1.14 mm². The variation in device size was facilitated by the design flexibility of the inkjet-printing process. The reported values of I_{DD} correspond to the current between the anode of the OPD and the source of the OTFT and are shown for different light intensities ranging from dark to 15 mW cm⁻² ($\lambda = 520$ nm). The observed increment of I_{DD} with higher light intensity can be solely attributed to the OPD response since the OTFTs from integrated devices showed negligible photo-induced current when tested individually (See Supplementary Fig. 5).

Since the OPD and OTFT devices are connected in series, their electrical characteristics as individual components define the operating point of the integrated device. Therefore, by varying the OPD size the characteristics of the integrated pixel can be tuned. When the OTFTs are operated in a saturation regime (Fig. 3a–c), the difference between the values of I_{DD} in the dark and at maximum illumination (ΔI), shows two orders of magnitude increase when the OPD size is decreased to 0.04 mm². This effect is due to the lower dark current exhibited by the smaller OPDs, which determines the floor of the pixel response. Under illumination, where the photoresistance of the OPD is the lowest, the maximum current is limited by the transistor thus remaining almost identical in the three cases. Figure 3d–f shows the transfer characteristics in the linear regime ($V_{DD} = -1$ V). In contrast to the saturation regime, the linear regime achieves a larger ΔI for each corresponding OPD sizes. In this case, we observed a three order of magnitude increase when comparing the largest to the smallest OPD active area. This can be explained by the change of operational regime. As part of our study, we measured ΔI as a function of the operational voltage by varying both V_{GS} and V_{DD} from 0 to -10 V and normalized to the corresponding dark current (I_0) of each device (See Supplementary Fig. 6). From $V_{DD} = -10$ V to $V_{DD} = -1$ V the increase in device response (ΔI/I_0)
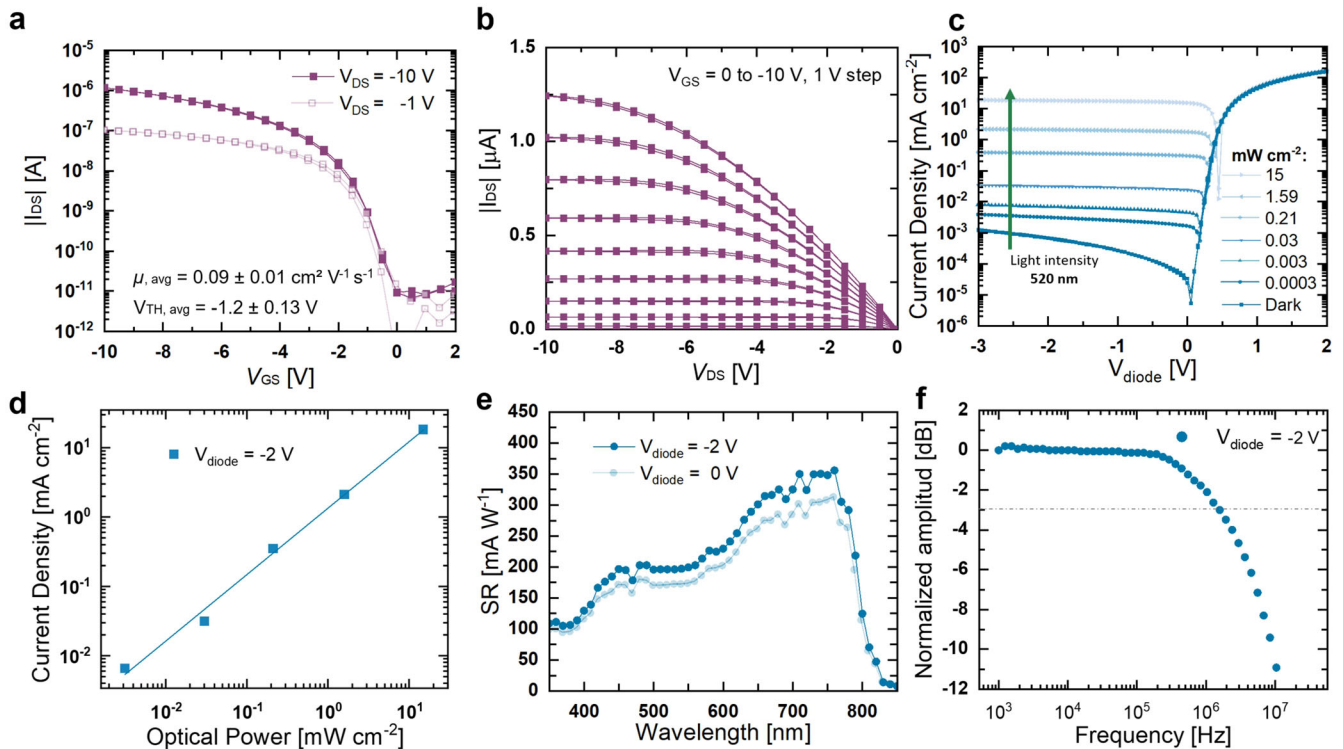
Fig. 2 Characteristics of individual OTFTs and OPDs. a Transfer characteristics of the individual transistors measured after integration. **b** Output characteristics of the individual transistors measured after integration. **c** J-V characteristics of the photodiodes measured after integration. The measurements were performed at different light intensities (as reported in mW cm^{-2}) and with a monochromatic light source ($\lambda = 520$ nm). **d** Devices response for different light intensities at -2 V. An LDR value of 89 dB was obtained. **e** Spectral responsivity of the device at 0 and -2 V. The peak responsivity reaches a value of 356 mA W^{-1} at -2 V. **f** Cut-off frequency measurement at -2 V. The 3$_{dB}$ cut-off frequency reaches a value above 1 MHz.

occurs mainly due to the transition into the linear regime of operation. In this regime, the output current increases substantially even for small increments in voltage resulting in higher relative changes in current as compared to the saturation regime. Furthermore, OPDs show higher dark current at higher V_{DD}, limiting the overall photoresponse of the pixel.

The findings from the full set of OPD sizes studied are summarized in Fig. 4a. The graph shows the relative change in photocurrent, i.e. $\Delta I/I_0$, at $V_{DD} = -1$ V exhibited by each integrated device as a function of OPD size and light intensity. Under the highest measured intensity (15 mW cm^{-2}) we observed a 70-fold difference in $\Delta I/I_0$ between devices with OPD sizes of 0.04 and 1.14 mm^2. Figure 4b presents $\Delta I/I_0$ and the power consumption of integrated pixels with different OPD sizes as a function of V_{DD} at a fixed $V_{GS} = -10$ V. The results show that lower V_{DD} values result in higher response and lower power consumption. We observed up to a 12-fold increase for $\Delta I/I_0$ and a decrease of 2 orders of magnitude for power consumption for an OPD size of 0.04 mm^2 when variating V_{DD} from -10 V to -1 V. Figure 4c correlates the power consumption and light sensitivity of the integrated devices and compares it to literature values of active Transistor/OPD pixel. The device sensitivity was defined as the slope of $\Delta I/I_0$ versus light intensity. In our case, the sensitivity was calculated from data extracted from Fig. 3 while for literature it was calculated from the available data when not provided in the manuscript (see Supplementary Table 1)[10,23,24,26,34–37]. When biased at $V_{DD} = -1$ V the power consumption of our devices goes from 100 nW down to 50 nW, while for $V_{DD} = -10$ V the value goes from 9 μW to 350 nW. These edge values correspond to the integrated devices with the biggest (1.14 mm^2) and smallest (0.04 mm^2) OPD footprints, respectively. In general, a clear trend towards higher sensitivity at lower power consumption can be appreciated by

lowering V_{DD}. Additionally, the reduction in OPD size further tuned the sensitivity toward higher values as indicated by the arrow direction in Fig. 4c. In comparison to other works, our devices achieved the lowest power consumption, reaching values below the μW range, and sensitivity among the highest reported so far. Concerning the device long-term stability, Supplementary Fig. 7 shows that $\Delta I/I_0$, measured at $V_{DD} = -1$ V, $V_{GS} = -10$ V, presented no degradation after the samples were stored for 13 months inside a glovebox in a nitrogen environment. The figure shows the transfer characteristics of three exemplary integrated pixels with an OPD active area of 0.11 mm^2 and its comparison to the values shown in Fig. 4a.

Characteristics of the integrated devices

The development of an integrated active-matrix relies not only on the electrical characteristics but also on the uniformity of performance among the devices. Figure 5a shows the histograms of the current in the dark and under illumination for 100 integrated pixels with an OPD size of 0.11 mm^2 ($V_{GS} = -10$ V, $V_{DD} = -1$ V). The pixels showed dark currents of 4.5 ± 1.8 nA and 105 ± 17 nA while illuminated (15 mW cm^{-2}, $\lambda = 520$ nm), demonstrating a robust fabrication process yielding highly reproducible devices for this pixel size. In contrast, the smallest devices (0.04 mm^2), even if better performant (See Fig. 4) posed challenges in the reliability of the printing process due to film formation issues where inhomogeneous wetting on the substrate was a critical burden for the smaller electrode structures. Supplementary Fig. 8, shows typical wetting issues that resulted in yields lower than 70%. Therefore, the integrated devices with an OPD size of 0.11 mm^2 were employed for further demonstrations.

The performance of the array under mechanical stress was tested by measuring $\Delta I/I_0$ ($V_{DD} = -1$ V, $V_{GS} = -10$ V) as a function
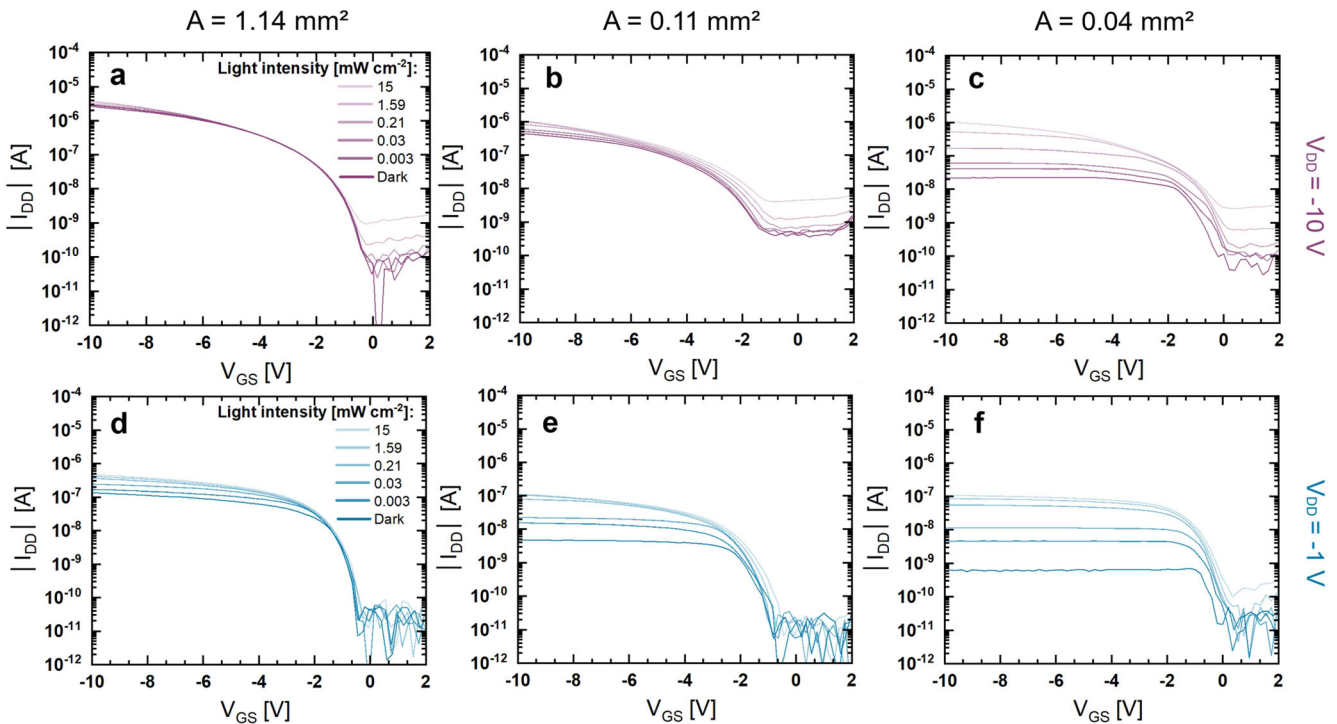
Fig. 3 Characteristics of integrated devices. a–c Transfer characteristics of the integrated devices in the saturation regime ($V_{DD} = -10$ V). The different integrated devices have an OPD size of 1.14, 0.11, and 0.04 mm², respectively. **d–f** Transfer characteristics of the integrated devices in the linear regime ($V_{DD} = -1$ V). The different integrated devices have an OPD size of 1.14, 0.11, and 0.04 mm², respectively.

of light intensity ($\lambda = 520$ nm) at different bending radiuses of the substrate (Fig. 5b). Values ranging from 5, 10, and 50 mm were chosen to emulate the bending radius of the sample when positioned on the hand, forearm or finger of a person (Fig. 5c). The radiuses were defined by semi-cylindrical test structures fabricated for this experiment (see the schematic of figure inset). It can be observed in Fig. 5b that regardless of the incident optical power, the device showed insignificant changes in current (<1%) when exposed to mechanical stress as compared to the flat condition. Thus we expect that the devices could be potentially utilized in real-life wearable applications.

Figure 5d shows real-time current measurements ($V_{DD} = -1$ V, $V_{GS} = -10$ V) in the dark and under illumination for a representative sample. The light source ($\lambda = 520$ nm) was turned on and off for intervals of 10 seconds while the output current to incident optical powers between 0.003 and 1.59 mW cm^{-2} was recorded. The devices showed a proportional change in light intensity reaching the same magnitude for each of the ten cycles and returning to the original value when the light stimuli was turned off. Thus, demonstrating the repeatability, reliability, and reversibility of the pixel photoresponse.

As a demonstration of a potential application, we performed real-time photo-plethysmography (PPG) measurements in transmission mode on a finger[52]. The schematic representation of the experiment can be seen in Fig. 5e, where the finger was placed on top of the sample while a red LED ($\lambda = 640$ nm) was used as an illumination source. After detecting the transmitted light, the sensor generates a dynamic current response that can be correlated to the pulsating blood flow. The results of three PPG measurements utilizing different pixels ($V_{DD} = -1$ V) are displayed in Fig. 5f. The graph shows the normalized response against time where the characteristic pulse pattern was observed and from which the heart rate frequency of the subject can be extracted (e.g., 67 beats per minute (bpm)). For comparison, the PPG measurement of one device obtained in the OTFT saturation regime ($V_{DD} = -10$ V) is also shown. In this case, the signal shows

less distinguishable peaks due to the lower sensitivity of the devices in this regime.

All-organic flexible active matrix

Figure 6 shows static and dynamic demonstrations of the performance of the 10×10 sensor matrix. In the first example (Fig. 6a) we carried out the recognition of static patterns through the use of a shadow mask. The experiment was performed on a flat sample (i.e., attached to a glass substrate) utilizing a patterned mask containing three apertures in the shape of a triangle, a cross, and a rectangle. These holes allow the incoming light (1.59 mW cm^{-2}, $\lambda = 520$ nm) to reach the set of pixels below them, while the rest of the pixels remain covered. As a result, pixels have different current values depending on their position within the mask. The color map shown in Fig. 6b shows $\Delta I/I_0$ for the 100 pixels ($V_{DD} = -1$ V, $V_{GS} = -10$ V). A signal contrast over three orders of magnitude was observed between covered and exposed pixel regions. The results show an accurate visualization of the geometrical figures and demonstrate that our active matrix is capable of spatial mapping.

For a dynamic demonstration, the matrix was placed on a test structure of radius = 10 mm resembling positioning the sample over the hand of a person, as displayed in Fig. 6c. A commercial laser pointer with monochromatic light ($\lambda = 640$ nm) was used to illuminate the sample. During the measurement the pointer was displaced across the sample to form different patterns as depicted in Fig. 6d. Pixel signals were collected via in-house developed readout electronics. The readout electronics employed allows to track a maximum of 5×5 pixels at once. The 25 pixels being recorded must be adjacent and their location within the matrix can be selected freely. In order to observe pixel responses over the complete (100-pixels) matrix, the 25-pixels window was selectively moved to different locations along the matrix to acquire data from different pixels and map the responses at different locations. The real-time data acquired during the measurement ($V_{DD} = -1$ V,
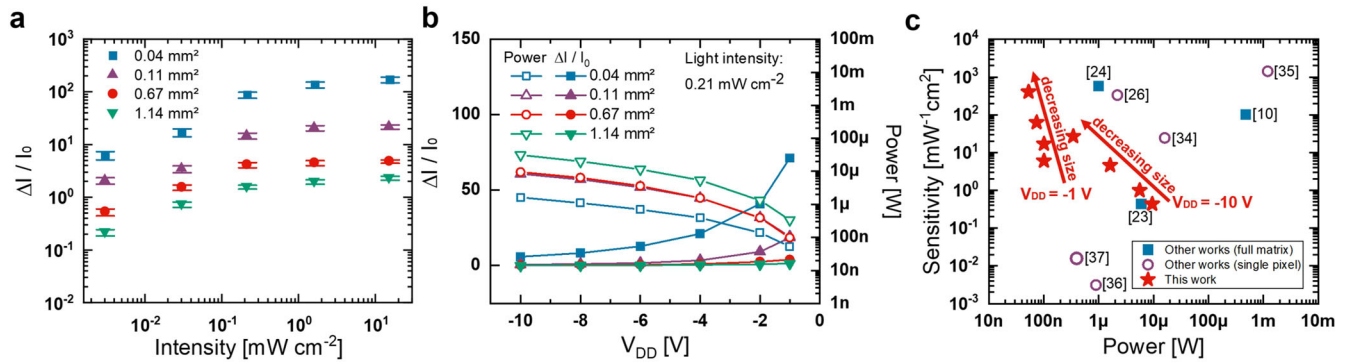
Fig. 4 Investigation on size and operational voltage. a Relative change in current versus light intensity for the integrated devices containing different OPD sizes, namely, 0.04. 0.11, 0.67, and 1.14 mm^2 ($V_{DD} = -1$ V; $V_{GS} = -10$ V). Error bars correspond to the standard deviation s.d. ($n = 3$). **b** Relative change in current and power consumption versus anode-source voltage V_{DD} at $V_{GS} = -10$ V for a light intensity of 0.21 mW cm^{-2}. **c** Sensitivity versus power consumption for our work $V_{GS} = -10$ V (red stars) and for other works found in the literature. Filled symbols represent works where a full matrix was also achieved and unfilled symbols represent works where only single pixels were presented.

$V_{GS} = -10$ V) for the illuminated pixels can be seen in Fig. 6e. It shows the real-time current response on the matrix for different pixels where the laser was positioned. As it can be seen, the motion path of the light spot can be tracked clearly. The real-time data of the non-illuminated pixels is shown in Supplementary Fig. 9. A video of the experiment can also be found in Supplementary Video 1. The demonstration of motion monitoring and spatial mapping highlights the potential of our active-matrix for a broad range of applications, and particularly, their suitability for fields such as wearable and flexible electronics.

In summary, we demonstrated the monolithic integration of an ultrathin and mechanically flexible active-matrix array comprised of 100 inkjet-printed OTFT/OPD optical sensors. Each pixel was fabricated by stacking over ten functional layers without the use of any subtractive techniques. Both the OTFTs and OPDs maintained state-of-the-art performance even after the complex integration process. The effects of scaling the geometrical footprint of the OPD yielded pixels with power consumptions down to 50 nW at one of the highest sensitivities reported to date for all-organic integrated sensors. Finally, we demonstrated the application potential of the active matrix by static and dynamic spatial sensing. The presented monolithic system encompasses high performance and device uniformity while being fabricated via an industrially relevant digital printing technique. Thus, our technology has the potential to fabricate complex circuitry in future sensing applications where freedom of design, low cost, performance, low weight, and flexibility are crucial.

METHODS

Fabrication of monolithic OTFT-OPD active-matrix array

(i) For the base substrate, a peel-off surfactant layer (Corning) was deposited by spin-coating on a 5×6 cm^2 glass substrate. On top of this, a ~2 μm parylene layer (KISCO Ltd.) was deposited by chemical vapor deposition (CVD) (OBT-PC300, OBANG Technology). (ii) The inkjet-printing process of the OTFTs (DMP 2850, Fujifilm Dimatix, 10 pL cartridge) took place over this parylene layer. Gate electrodes and word lines were inkjets printed using a 55 wt % Ag nanoparticle ink (Nanopaste NPS-JL, Harima Chemicals Inc.). The deposited silver was annealed at 120 °C for 30 min. (iii) Through CVD a second parylene layer (200 nm) was deposited to be used as a dielectric. (iv) Source/drain electrodes and bit lines formed by the same Ag nanoparticle ink as the gate were deposited on top of the dielectric layer and annealed at 120 °C for 30 min. Additionally, a Self-assembled monolayer (SAM) solution consisting of Pentafluorobenzenethiol (PFBT) in isopropanol (2.5 μL/mL) was used to modify the work function of the source

and drain electrodes. To this purpose, the samples were submerged into the SAM solution for 5 min and then rinsed with isopropanol. (v) An air-pulse dispenser (350PC, MUSASHI ENG.) was used to pattern and deposit the semiconductor material. First, a 1 wt % solution of Teflon (AF1600, DuPont) in perfluorotributylamine (Fluorinert FC-43, 3 M) was printed in rectangular-shaped reservoirs to define the OTFT active areas. After deposition, the Teflon reservoirs were annealed at 60 °C for 30 min and the semiconductor solution of poly(N-alkyl diketopyrrolopyrrole dithienylthieno-[3,2-b]thiophene) DPP-DTT (M37, Ossila Inc.) dissolved in chlorobenzene (2 mg/mL) was printed inside the reservoirs with the air-pulse dispenser and annealed at 100 °C for 30 min. The sample was then submerged in perfluorotributylamine for 5 min to remove the Teflon-based reservoirs. Afterward, a 1:4 solution of Cytop (CTL-809M, Asahi Glass) in CT Solv. 180 was spin-coated on top (2500 rpm, 30 s) and annealed at 100 °C for 30 min. (vi) An additional parylene layer (2 μm) was deposited via CVD to be used as an interlayer and as a base for the monolithic deposition of the OPDs. (vii) Via holes to connect the electrodes of different layers were made with a pulsed laser (shot pulse width = 2.5 ns, $\lambda = 532$ nm). (viii) All via holes were filled by inkjet-printed Ag nanoparticle ink. Further details about the fabrication process including temperature and nozzle settings are explained in a previous work[9]. (ix) A one-minute Argon plasma treatment was performed on the parylene interlayer of the samples to adjust the surface energy prior to the deposition of the OPDs. (x) The inkjet-printing process for the OPDs (Pixdro LP50 (MeyerBurger), 10 pL 16 nozzle Fujifilm Dimatix cartridges) took place over the top parylene interlayer. Silver electrodes (100 nm) were inkjet printed using a 30–35 wt% Ag nanoparticle ink (Sigma-Aldrich TGME Silver Dispersion) and annealed at 120 °C for 10 min. (xi) Subsequently, SnO$_2$ hole-blocking layers (25 nm) were inkjet printed on top of each silver electrode by employing a 2:1 solution of commercial SnO$_2$ nanoparticle ink (Avantama N-31) and diethylene glycol (DEG). The sample was then annealed at 120 °C for 5 min. (xii) The active layer blend was processed by preparing separate solutions of poly(3-hexylthiophene) P3HT (RIEKE Metals) and the small-molecular 5,5′-[[4,4,9,9-Tetraoctyl-4,9-dihydro-s-indaceno[1,2-b:5,6-b′]dithiophene-2,7-diyl]bis(2,1,3-benzothiadiazole-7,4-diylmethylidyne)]bis[3-ethyl-2-thioxo-4-thia-zolidinone] IDTBR (1-MATERIALS) in o-dichlorobenzene (20 mg/mL) and subsequent mixing of the solutions (1:1) by stirring overnight. Afterward, the layers were inkjet-printed (250 nm) and annealed at 140 °C for 10 min inside an N$_2$-filled glovebox (O$_2$ and H$_2$O < 0.1 ppm). (xiii) To complete the OPD stack, a transparent electrode (300 nm) based on PEDOT:PSS (Clevios FHC-Solar Heraeus) with 0.3 vol% of Zonyl FS-300 (Fluka analytical) was inkjet printed on top of the active layers and annealed at 120 °C
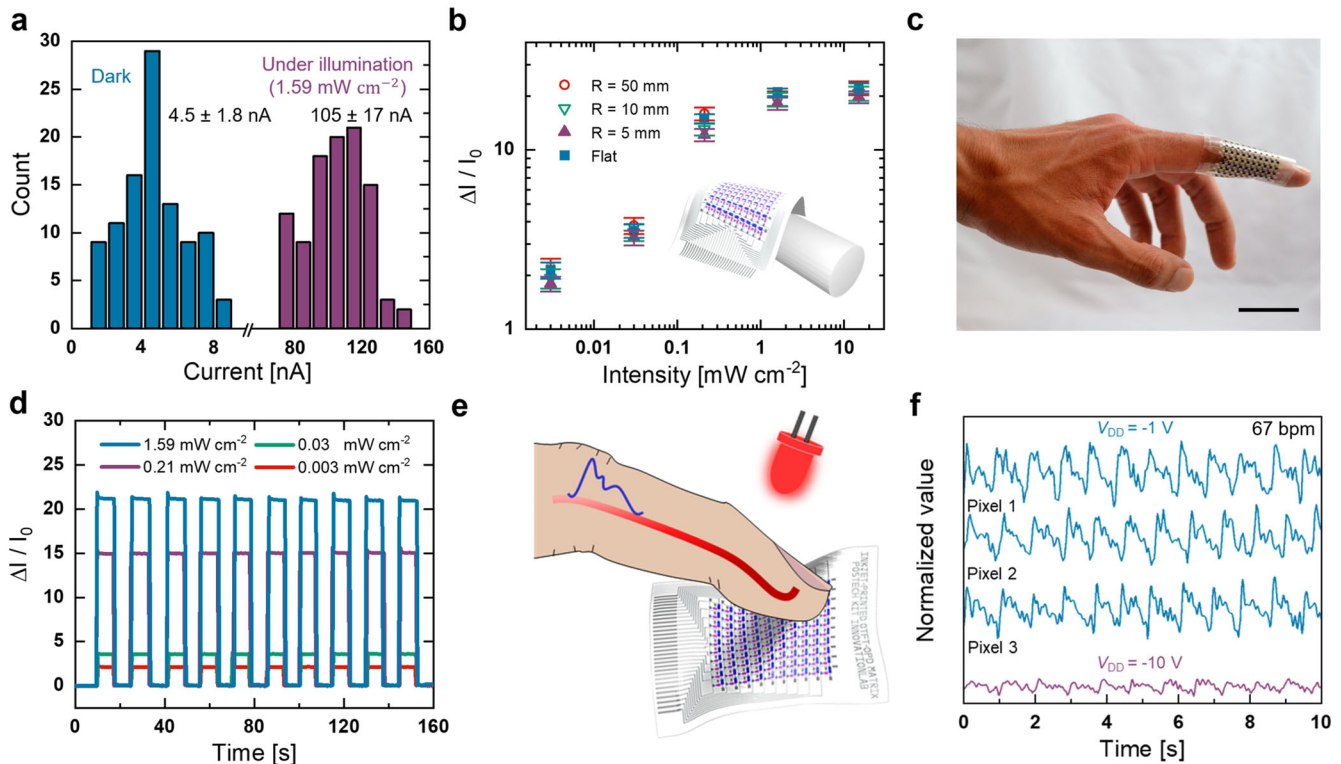
Fig. 5 Characterization of integrated devices. a Current distribution of 100 integrated devices. **b** Bending tests on integrated devices. The relative change in current is plotted against the light intensity for different bending radius. The bending radius (R) is defined by different test structures fabricated for this experiment. Inset shows a schematic of the sample and a test structure. Error bars correspond to the standard deviation s.d. ($n = 3$). **c** Photograph of flexible active-matrix sample conforming to a finger (scale bar = 3 cm). **d** Dynamic current response. The relative change in current is plotted against time for different light intensities. Illumination was turned on and off for intervals of 10 s while the output current was recorded in real-time. **e** Schematic of finger pulse measurement in transmission mode. **f** Response obtained from finger pulse measurement in the saturation ($V_{DD} = -10\,V$) and linear ($V_{DD} = -1\,V$) regimes. A heartbeat value of 67 bpm was calculated from the measurements.

for 5 min. The thicknesses of the printed layers were determined by profilometry (Veeco, Dektak 150). Cartridge waveforms were developed independently for each layer and all ink solutions used for the OPD stack were filtered with a 0.45 μm polyvinylidene fluoride (PVDF) filter prior to deposition.

Device characterization

Current-voltage (I-V) measurements were performed by employing an Agilent 4155 C semiconductor parameter analyzer. For I-V measurements performed under illumination, a green LED ($\lambda = 520\,nm$) was used as a light source powered via a Keithley 2636 A source measure unit (SMU). Neutral density (ND) filters (Thorlabs NDUVxxA/NE5xxB) were employed to adjust the light intensity.

Responsivity measurements were performed using a 450 W OSRAM XBO Xenon discharge lamp as a light source and a monochromator (Acton SP-2150i) was used to selectively filter the light source. The light was then modulated with a chopper wheel to a frequency of 173 Hz. An amplifier (Femto DHPCA-100) was used to amplify the signal and the output signal was measured with an SR830 lock-in amplifier.

The bandwidth was characterized by measuring the transient current under illumination with a square-light signal of varying frequency. An oscilloscope (Agilent DSO 6102 A) was used to record the current while an Oxxius LBX520 laser was used as a light source. A function generator (Agilent 33522 A) was used to modulate the light.

To measure the responsivity and bandwidth of the OPDs, a special layout was required. The layout was designed to match the contact pins of the sample-holder belonging to the EQE and

bandwidth probe station (Supplementary Fig. 10). The design rules used to integrate the devices within this layout remain the same as those employed on the full matrix.

The noise spectral density (Sn) was measured by recording the dark current in a custom-made shielded box to avoid the in-coupling of pickup-noise. The signal was amplified with a trans-impedance amplifier (TIA, FEMTO DLPCA-200) connected directly to the box and current values were recorded with an SMU (Keithley 2636 A). A Hann window function was multiplied to account for digitization errors and the data was Fourier-transformed into reciprocal space to extract the frequency-dependency of the noise. An isolated voltage source (SIM928, SRS) was used to apply $-2\,V$ reverse bias via a BNC connection. To calculate D^* we used the measured SR at 760 nm, Sn, as well as the area of the OPD.

PPG measurements in transmission mode were recorded using a Keithley 2636 A SMU via a Labview-programmed user interface. A red LED ($\lambda = 640\,nm$) was used as a light source and powered via a second Keithly 2636 A SMU.

The spatial mapping of the matrix for the dynamic demonstration was done using custom-built readout electronics by measuring the current of each pixel. Signals were collected via analog-to-digital converters (ADC) and processed using MATLAB. More specifically, we have used a 115200 bps-UART and 12-bit-ADC chip for the scanning electronics. The electronics scans the selected 5×5 square grid in the array at 30 Hz (30 frames per second), and the signals at each pixel were recorded at 30 Hz. As we used one ADC for the array, the ADC collected signals at 750 Hz (30 Hz × 25 pixels). The biases used are $V_{GS} = -10$ for a word line, and $V_{DD} = -10\,V$ or $-1\,V$ for a bit line.
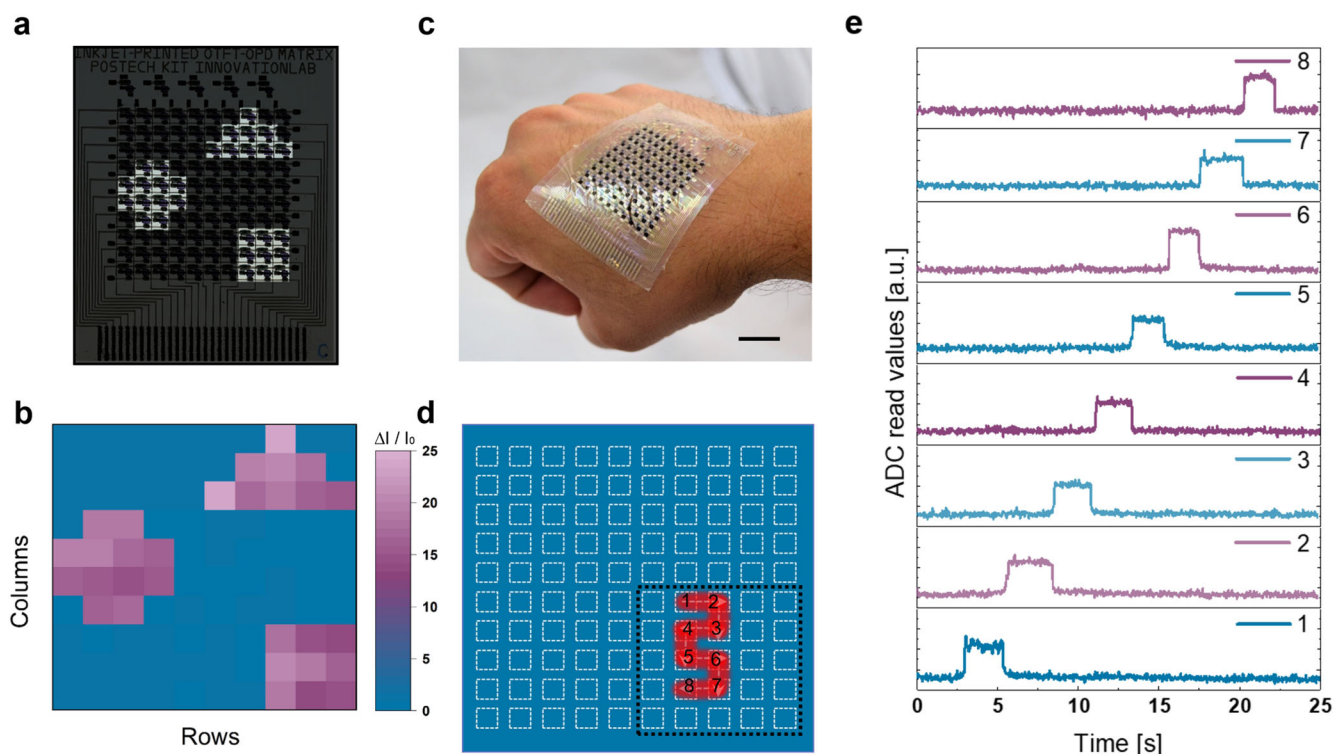
Fig. 6   Active-matrix demonstration. a Photograph of the active matrix covered by a schematic of the patterned mask layout used during the static demonstration measurement. **b** Mapping of the light response across the 10×10 active matrix during static demonstration measurement. The relative change in current is shown for each pixel. Different colors indicate different responses. **c** Photograph of flexible active-matrix sample placed on top of a hand (scale bar = 2 cm). **d** Schematic of the movement of a point light source over the active matrix. The displacement of light forms different patterns. **e** Real-time current response over the active-matrix while the light was being displaced over the sample. The particular set of data shown here corresponds to the labeled pixels at the bottom-right pattern in Fig. **d**. The complete set of data is also shown as a video in the supporting information.

Ethics declarations

This study was approved by the Institutional Review Board of Pohang University of Science and Technology and conducted according to the ethical principles for medical research on human subjects of the Declaration of Helsinki (PIRB-2021-E009). We have obtained informed consent from all participants.

DATA AVAILABILITY

The data that support the findings of this study are available from the corresponding authors upon reasonable request.

CODE AVAILABILITY

The underlying code for this study is not publicly available but may be made available to qualified researchers on reasonable request from the corresponding author.

REFERENCES
1. Nabet, B. *Photodetectors: Material, Devices and Applications* (Elsevier-Woodhead, 2016).
2. Yun, I. *Photodiodes - From Fundamentals to Applications* (InTechOpen, 2012).
3. Khan, S., Lorenzelli, L. & Dahiya, R. S. Technologies for printing sensors and electronics over large flexible substrates: a review. *IEEE Sens. J.* **15**, 3164–3185 (2015).
4. Inzelberg, L. et al. Printed facial skin electrodes as sensors of emotional affect. *Flex. Print. Electron.* **3**, 045001 (2018).
5. Vega-Colado, C. et al. An all-organic flexible visible light communication system. *Sensors* **18**, 3045 (2018).
6. Lee, S. H. et al. Toward color-selective printed organic photodetectors for high-resolution image sensors: from fundamentals to potential commercialization. *Mater. Sci. Eng. Rep.* **147**, 100660 (2022).
7. Mawlong, L. P. L. & Ahn, J.-H. 3D-structured photodetectors based on 2D transition-metal dichalcogenide. *Small Struct.* **3**, 2100149 (2022).
8. Park, S. et al. Ultraflexible near-infrared organic photodetectors for conformal photoplethysmogram sensors. *Adv. Mater.* **30**, 1802359 (2018).
9. Baek, S. et al. Spatiotemporal measurement of arterial pulse waves enabled by wearable active-matrix pressure sensor arrays. *ACS Nano* **16**, 368–377 (2022).
10. Takahashi, T. et al. Carbon nanotube active-matrix backplanes for mechanically flexible visible light and X-ray imagers. *Nano Lett.* **13**, 5425–5430 (2013).
11. Perevedentsev, A. et al. Polarization-sensitive photodetectors based on directionally oriented organic bulk-heterojunctions. *Adv. Opt. Mater.* **10**, 2102397 (2022).
12. Catania, F., De Souza Oliveira, H., Lugoda, P., Cantarella, G. & Münzenrieder, N. Thin-film electronics on active substrates: review of materials, technologies and applications. *J. Phys. D: Appl. Phys.* **55**, 323002 (2022).
13. Strobel, N. et al. Color-selective printed organic photodiodes for filterless multi-channel visible light communication. *Adv. Mater.* **32**, 1908258 (2020).
14. Simone, G. et al. On the origin of dark current in organic photodiodes. *Adv. Opt. Mater.* **8**, 1901568 (2020).
15. Fuentes-Hernandez, C. et al. Large-area low-noise flexible organic photodiodes for detecting faint visible light. *Science* **370**, 698–701 (2020).
16. Pierre, A. & Arias, A. C. Solution-processed image sensors on flexible substrates. *Flex. Print. Electron.* **1**, 043001 (2016).
17. Baek, S., Kwon, J., Mano, T., Tokito, S. & Jung, S. A flexible 3D organic preamplifier for a lactate sensor. *Macromol. Biosci.* **20**, 2000144 (2020).
18. Strobel, N., Seiberlich, M., Eckstein, R., Lemmer, U. & Hernandez-Sosa, G. Organic photodiodes: printing, coating, benchmarks, and applications. *Flex. Print. Electron.* **4**, 043001 (2019).
19. Mittal, P., Yadav, S. & Negi, S. Advancements for organic thin film transistors: structures, materials, performance parameters, influencing factors, models, fabrication, reliability and applications. *Mater. Sci. Semicond. Process.* **133**, 105975 (2021).
20. Simone, G., Dyson, M. J., Meskers, S. C. J., Janssen, R. A. J. & Gelinck, G. H. Organic photodetectors and their application in large area and flexible image sensors: the role of dark current. *Adv. Funct. Mater.* **30**, 1904205 (2020).

21. Eckstein, R. et al. Fully digitally printed image sensor based on organic photo-diodes. *Adv. Opt. Mater.* **6**, 1701108 (2018).
22. Lee, K. H. et al. An almost transparent image pixel with a pentacene/ZnO pho-todiode, a pentacene thin-film transistor, and a 6,13-pentacenequinone phos-phor layer. *Adv. Mater.* **23**, 1231–1236 (2011).
23. Someya, T. et al. Integration of organic FETs with organic photodiodes for a large area, flexible, and lightweight sheet image scanners. *IEEE Trans. Electron Devices* **52**, 2502–2511 (2005).
24. Gelinck, G. H. et al. X-ray imager using solution processed organic transistor arrays and bulk heterojunction photodiodes on thin, flexible plastic substrate. *Org. Electron.* **14**, 2602–2609 (2013).
25. Jia, X., Fuentes-Hernandez, C., Chou, W. F. & Kippelen, B. Organic photodetector with built-in amplification for the detection of visible light with low optical power. *Org. Electron.* **90**, 106064 (2021).
26. Wang, H. et al. A retina-like dual band organic photosensor array for filter-free near-infrared-to-memory operations. *Adv. Mater.* **29**, 1701772 (2017).
27. Nausieda, I. et al. An organic active-matrix imager. *IEEE Trans. Electron Devices* **55**, 527–532 (2008).
28. Jiang, Z. et al. Ultraflexible integrated organic electronics for ultrasensitive pho-todetection. *Adv. Mater. Technol.* **6**, 2000956 (2021).
29. Park, J. H. et al. Photo-stable organic thin-film transistor utilizing a new indolo-carbazole derivative for image pixel and logic applications. *Adv. Funct. Mater.* **24**, 1109–1116 (2014).
30. Maiellaro, G. et al. Ambient light organic sensor in a printed complementary organic TFT technology on flexible plastic foil. *IEEE Trans. Circuits Syst. I Regul. Pap.* **61**, 1036–1043 (2014).
31. Lee, K. H. et al. Semi-transparent organic/inorganic hybrid photo-detector using pentacene/ZnO diode connected to pentacene transistor. *Org. Electron.* **12**, 1103–1107 (2011).
32. Wang, H. et al. Three-component integrated ultrathin organic photosensors for plastic optoelectronics. *Adv. Mater.* **28**, 624–630 (2016).
33. Renshaw, C. K., Xu, X. & Forrest, S. R. A monolithically integrated organic pho-todetector and thin film transistor. *Org. Electron.* **11**, 175–178 (2010).
34. Tong, X. & Forrest, S. R. An integrated organic passive pixel sensor. *Org. Electron.* **12**, 1822–1825 (2011).
35. Prevot, P.-H., Alvares, D., Micolich, A., Lovell, N. & Ladouceur, F. An all-organic active pixel photosensor featuring ion-gel transistors. *J. Org. Semicond.* **3**, 8–13 (2015).
36. Jeong, S. W. et al. The vertically stacked organic sensor-transistor on a flexible substrate. *Appl. Phys. Lett.* **97**, 253309 (2010).
37. Swathi, K. & Narayan, K. S. Image pixel device using integrated organic electronic components. *Appl. Phys. Lett.* **109**, 193302 (2016).
38. Salaoru, I., Maswoud, S. & Paul, S. Inkjet printing of functional electronic memory cells: a step forward to green electronics. *Micromachines* **10**, 417 (2019).
39. Kwon, J., Jung, S., Baek, S., Lee, Y. & Tokito, S. Layout-to-Bitmap conversion and design rules for inkjet-printed large-scale integrated circuits. *Langmuir* **37**, 10692–10701 (2021).
40. Lee, Y. et al. Reliable inkjet contact metallization on printed polymer semi-conductors for fabricating staggered TFTs. *Appl. Phys. Lett.* **116**, 153301 (2020).
41. Schlisske, S. et al. Surface energy patterning for ink-independent process opti-mization of inkjet-printed electronics. *Flex. Print. Electron.* **6**, 015002 (2021).
42. Baek, S., Bae, G. Y., Kwon, J., Cho, K. & Jung, S. Flexible pressure-sensitive contact transistors operating in subthreshold regime. *ACS Appl. Mater. Interfaces* **11**, 31111–31118 (2019).
43. Strobel, N., Seiberlich, M., Rödlmeier, T., Lemmer, U. & Hernandez-Sosa, G. Non-fullerene-based printed organic photodiodes with high responsivity and megahertz detection speed. *ACS Appl. Mater. Interfaces* **10**, 42733–42739 (2018).
44. Gasparini, N. et al. Visible and near-infrared imaging with nonfullerene-based photodetectors. *Adv. Mater. Technol.* **3**, 1800104 (2018).
45. Liess, A. et al. Ultranarrow bandwidth organic photodiodes by exchange nar-rowing in merocyanine H- and J-aggregate excitonic systems. *Adv. Funct. Mater.* **29**, 1805058 (2019).
46. Sung, M. J., Yoon, S., Kwon, S. K., Kim, Y. H. & Chung, D. S. Synthesis of phe-nanthro[1,10,9,8-cdefg]carbazole-based conjugated polymers for green-selective organic photodiodes. *ACS Appl. Mater. Interfaces* **8**, 31172–31178 (2016).
47. Biele, M. et al. Spray-coated organic photodetectors and image sensors with silicon-like performance. *Adv. Mater. Technol.* **4**, 1800158 (2019).
48. Cesarini, M., Brigante, B., Caironi, M. & Natali, D. Reproducible, high performance fully printed photodiodes on flexible substrates through the use of a poly-ethylenimine interlayer. *ACS Appl. Mater. Interfaces* **10**, 32380–32386 (2018).
49. Yoon, S., Ha, Y. H., Kwon, S. K., Kim, Y. H. & Chung, D. S. Fabrication of high performance, narrowband blue-selective polymer photodiodes with dialkoxynapht halene-based conjugated polymer. *ACS Photonics* **5**, 636–641 (2018).
50. Tordera, D. et al. A high-resolution thin-film fingerprint sensor using a printed organic photodetector. *Adv. Mater. Technol.* **4**, 1900651 (2019).
51. Lyons, D. M. et al. Narrow band green organic photodiodes for imaging. *Org. Electron.* **15**, 2903–2911 (2014).
52. Přibil, J., Přibilová, A. & Frollo, I. Comparative measurement of the PPG signal on different human body positions by sensors working in reflection and transmis-sion modes. *Eng. Proc.* **2**, 69 (2020).

AUTHOR CONTRIBUTIONS
L.A.R.-P. and S.B. fabricated the samples. L.A.R.-P., S.B., and N.S. contributed to the design of the integration layout. N.S. supported the design of the circuit board. L.A.R.-P. and S.B. characterized the devices and performed the demonstrations. M.S. and K.X. wrote programming scripts and assisted with modifications to measurement setups. S.-m.P. designed and provided the matrix readout electronics. L.A.R.-P., S.B., and G.H.-S. analyzed the data and discussed the results. L.A.R.-P., S.B., and G.H.-S. wrote the manuscript. All authors reviewed and approved the manuscript. G.H.-S., S.J., and U.L. supervised the research. G.H.-S. and S.J. conceived the research project and coordinated the research. L.A.R.-P. and S.B. contributed equally to this work.

FUNDING
Open Access funding enabled and organized by Projekt DEAL.

COMPETING INTERESTS
The authors declare no competing interests.

ADDITIONAL INFORMATION
Supplementary information The online version contains supplementary material available at https://doi.org/10.1038/s41528-023-00242-7.

Correspondence and requests for materials should be addressed to Sungjune Jung or Gerardo Hernandez-Sosa.

Reprints and permission information is available at http://www.nature.com/reprints

Publisher's note Springer Nature remains neutral with regard to jurisdictional claims in published maps and institutional affiliations.